2015

Measurement of InAsSb bandgap energy and InAs/InAsSb band edge positions using spectroscopic ellipsometry and photoluminescence spectroscopy

P. T. Webster
Arizona State University

N. A. Riordan
Arizona State University

S. Liu
Arizona State University

E. H. Steenbergen
U. S. Air Force Research Laboratory, AFRL/RXAN, Wright Patterson, Ohio

R. A. Synowicki
J. A. Woollam Co., Inc., 645 M. Street, Suite 102, Lincoln, Nebraska

See next page for additional authors

Measurement of InAsSb bandgap energy and InAs/InAsSb band edge positions using spectroscopic ellipsometry and photoluminescence spectroscopy

P. T. Webster,[1] N. A. Riordan,[1] S. Liu,[1] E. H. Steenbergen,[2] R. A. Synowicki,[3] Y.-H. Zhang,[1] and S. R. Johnson[1,a)]

[1]*Center for Photonics Innovation and School of Electrical, Computer, and Energy Engineering, Arizona State University, Tempe, Arizona 85287, USA*
[2]*U. S. Air Force Research Laboratory, AFRL/RXAN, Wright Patterson, Ohio 45433, USA*
[3]*J. A. Woollam Co., Inc., 645 M. Street, Suite 102, Lincoln, Nebraska 68508, USA*

(Received 1 September 2015; accepted 19 December 2015; published online 31 December 2015)

The structural and optical properties of lattice-matched $InAs_{0.911}Sb_{0.089}$ bulk layers and strain-balanced InAs/$InAs_{1-x}Sb_x$ ($x \sim 0.1$–0.4) superlattices grown on (100)-oriented GaSb substrates by molecular beam epitaxy are examined using X-ray diffraction, spectroscopic ellipsometry, and temperature dependent photoluminescence spectroscopy. The photoluminescence and ellipsometry measurements determine the ground state bandgap energy and the X-ray diffraction measurements determine the layer thickness and mole fraction of the structures studied. Detailed modeling of the X-ray diffraction data is employed to quantify unintentional incorporation of approximately 1% Sb into the InAs layers of the superlattices. A Kronig-Penney model of the superlattice miniband structure is used to analyze the valence band offset between InAs and InAsSb, and hence the InAsSb band edge positions at each mole fraction. The resulting composition dependence of the bandgap energy and band edge positions of InAsSb are described using the bandgap bowing model; the respective low and room temperature bowing parameters for bulk InAsSb are 938 and 750 meV for the bandgap, 558 and 383 meV for the conduction band, and −380 and −367 meV for the valence band. [http://dx.doi.org/10.1063/1.4939293]

I. INTRODUCTION

The strain-balanced InAs/InAsSb type-II superlattice exhibits many favorable and unique properties to justify its utilization in high-performance infrared optoelectronic devices; however, accurate modeling of the superlattice miniband structure necessary for design optimization relies on accurate knowledge of the InAsSb bandgap and band edge positions.[1,2] A definitive measurement of the bandgap energy of a ternary semiconductor alloy is difficult to obtain due in part to the fact that the alloy is generally not lattice-matched to the underlying substrate. Consequently, the band edge energies of the alloy are modified depending on whether the lattice is coherently strained or partially relaxed. The bandgap energy can be measured in relaxed material, but even very thick layers can retain some residual strain and the misfit dislocations that result are highly detrimental to the optical quality of the material. Alternatively, if strain and confinement effects can be accurately accounted for, then the bandgap energy can be determined from thin layers that accommodate the lattice strain; however, small bandgap alloys are particularly difficult to assess with this method, as confinement and strain effects become increasingly more significant as the bandgap energy is reduced. Nevertheless once these measurements are made on a set of samples, the bandgap energy of the alloy is generally expressed as a function of mole fraction and fit to a second order polynomial. The second order polynomial coefficient is referred to as the bowing parameter[3] and is reported by many authors.

An extensive literature review indicates that a commonly accepted bandgap bowing parameter for InAsSb is 670 meV;[4] however, much of the work referenced therein assumes that the materials measured are fully relaxed. If the material is not fully relaxed, the residual compressive strain will increase the bandgap energy resulting in an underestimation of the bandgap bowing parameter of the free-standing material. The minimum bandgap energy that can be achieved with a 670 meV bandgap bowing parameter is 146 meV (8.5 μm wavelength), which occurs for a Sb mole fraction of 0.636. However, in 1988 emission at wavelengths as long as 10 μm are reported for photoluminescence[5] and photoconductance[6] measurements of metamorphic InAsSb layers grown by molecular beam epitaxy on GaAs substrates, indicating that the bandgap bowing parameter is greater than 670 meV. More recently, 1 μm thick lattice-matched InAsSb layers have been grown on metamorphic AlGaInSb buffers by molecular beam epitaxy,[7] and a 870 meV bandgap bowing parameter is obtained from photoluminescence measurements at low temperature.[8] Reciprocal space maps and transmission electron microscopy techniques verified that the InAsSb layers are unstrained and without ordering.

A comprehensive literature review finds a large spread in the reported values of the InAsSb band edge positions and describes how precise estimates of the conduction and valence band edge positions rely on accurate knowledge of the materials bandgap bowing parameter.[9] In Section II, the low and

a)Electronic mail: shane.johnson@asu.edu

room temperature bandgap energies of $InAs_{0.911}Sb_{0.089}$ are, respectively, determined using photoluminescence and ellipsometry measurements, and these values are used to determine the low and room temperature bandgap bowing parameters of InAsSb. In Section III, the low and room temperature ground state transition energies of strain-balanced InAs/InAsSb superlattices are, respectively, determined using photoluminescence and spectroscopic ellipsometry. In Section IV, the InAs/InAsSb band offset is a free parameter in the analysis and comparison of the superlattice ground state transition energies measured in Section III, and the band offset of each superlattice sample is determined using a Kronig-Penney model. The measured band offsets along with the measured InAsSb bandgap bowing parameter determine the conduction and valence band bowing parameters of InAsSb.

II. ELLIPSOMETRY AND PHOTOLUMINESCENCE OF $InAs_{0.911}Sb_{0.089}$

The bulk InAsSb layer used to determine the bandgap bowing parameter of InAsSb is precisely lattice-matched to GaSb. The sample is grown by molecular beam epitaxy at 430 °C on a quarter of a 50 mm (100) ± 0.1° GaSb substrate, consists of a 500 nm thick $InAs_{0.911}Sb_{0.089}$ layer sandwiched between two 10 nm thick AlSb layers that provide carrier confinement for photoluminescence experiments, and the entire structure is capped with 10 nm of GaSb to prevent oxidation of the upper AlSb layer. X-ray diffraction measurements are performed using a PANalytical X'Pert PRO Materials Research Diffractometer. The incident beam optics consist of an X-ray mirror and a 2-crystal Ge (220) 4-bounce monochromator with a 0.25° divergence slit, and a 1/4 in. width mask is used to probe a large area of the sample. The diffracted beam optics utilize a triple axis monochromator and a 0.50° slit placed before the detector. The precise lattice-matched composition is determined from coupled ω-2θ X-ray diffraction scans from the (004)-planes of a series of calibration samples shown in the inset of Fig. 1. The mole fractions are determined using the commercial dynamical X-ray diffraction software X'pert Epitaxy;[10] Sb mole fractions of 0.093 and 0.087 are determined from the diffraction patterns of calibration samples 1 and 2 in the figure (dotted and dotted–dashed black curves), and the lattice-matched mole fraction of 0.0891 is inferred from the diffraction pattern of the lattice-matched sample (solid black curve) as the substrate and layer diffraction peaks are coincident in this sample and are no broader than the diffraction peak from a bare GaSb wafer (solid grey curve). Pendellösung fringes which arise as a result of the 10 nm thick AlSb layers that sandwich the lattice-matched InAsSb attest that the layer thickness is 500 ± 20 nm. The same piece of the $InAs_{0.911}Sb_{0.089}$ sample on which X-ray diffraction is performed is then cleaved into photoluminescence and ellipsometry samples, and the latter is backside roughened with 320 grit sandpaper to diffusely scatter any light that may reach the backside of the semitransparent GaSb wafer during the ellipsometry measurement.

The optical constants of the $InAs_{0.911}Sb_{0.089}$ layer are measured at room temperature using an infrared variable angle spectroscopic ellipsometer[11] that covers the 30 to 800 meV (40–1.55 μm wavelength) photon energy range. The optical constants are obtained from the measured ellipsometric parameters Ψ and Δ, using the basic wavelength-by-wavelength (point-by-point) analysis method[12] in the same manner as in Ref. 2. This results in the actual measured optical constants unmodified by any particular fitting or smoothing model such as the general oscillator model and its various functional forms. The extinction coefficient k and photon wavelength λ are used to calculate the absorption coefficient $\alpha = 4\pi k/\lambda$. As the absorption coefficient is proportional to the optical joint density of states, its first derivative as function of energy is used to identify the maximum change in the optical joint density of states and hence the energy at which the onset of optical transitions involving the continuum band edges occurs. The absorption coefficient of $InAs_{0.911}Sb_{0.089}$ is presented in Fig. 1 alongside its first derivative that shows two distinct absorption features occurring at 225 and 277 meV. The 225 meV feature is the cutoff in the below bandgap absorption, which is the point at which absorption in the 500 nm thick layer is no longer observable. The 277 meV feature is onset of optical transitions involving the continuum band edges of the fundamental bandgap.

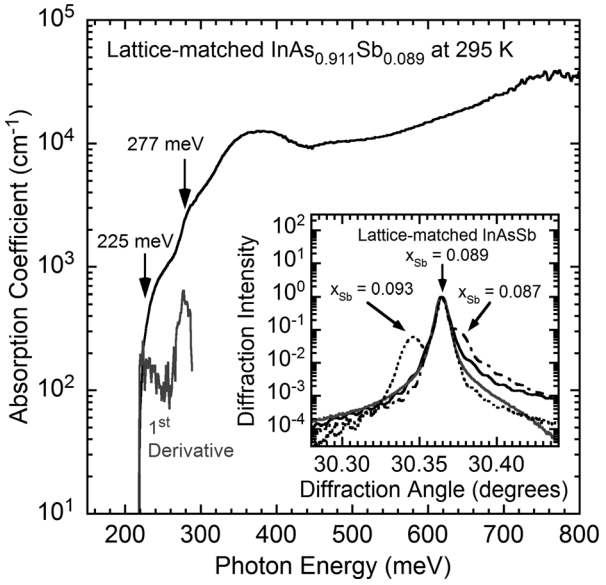

FIG. 1. Absorption coefficient (black curve) of $InAs_{0.911}Sb_{0.089}$ and its first derivative (grey curve). Two absorption onsets are identified from two peaks in the first derivative, one at the onset of sample absorption (225 meV) and one at the bandgap energy (277 meV). Inset shows coupled ω-2θ X-ray diffraction scans from the (004)-planes of a series of calibration samples (dotted and dotted-dashed black curves) used to precisely hone in on the composition of the lattice-matched InAsSb sample (solid black curve). X-ray diffraction from a bare GaSb wafer is shown for comparison (solid grey curve).

Photoluminescence is measured as a function of temperature (15–295 K) and pump power (0.1–200 mW) using a Nicolet Instrument Corporation Magna-IR 760 Fourier transform infrared spectrometer and an 808 nm pump laser with spot diameter of 183 μm. The corresponding pump power density at the upper InAsSb layer interface is 0.133 to 265 W cm^{-2}, and the corresponding carrier excitation density in the InAsSb layer is 1×10^{22} to 2×10^{25} cm^{-3} s^{-1}. The bandgap energy is determined at each temperature using two

methods, both of which are demonstrated using the 30 K photoluminescence spectra plotted in Fig. 2. In the peak method, the bandgap energy (E_p) is identified as the photoluminescence peak energy minus $kT/2$.[13] This method assumes an idealized parabolic band cutoff in the density of states of bulk material, ignoring the impact of localized states found near the continuum band edges in real material.[14,15] In the photoluminescence first derivative method, the bandgap energy (E_g) is identified as the maximum of the first derivative of the photoluminescence spectra (shown in the Fig. 2 inset), which identifies the maximum change in the optical joint density of states at the bandgap energy. Note that both methods correctly identify the bandgap energy in the idealized case of a perfectly sharp band edge cutoff specified by the parabolic band model.

Two injection level regimes are indicated in Fig. 2; at high injection, the photoluminescence peak blue shifts with increasing excitation density, while at low injection the photoluminescence peak energy is independent of excitation density. When identifying the bandgap energy using the peak minus $kT/2$ method, the low injection photoluminescence peak position is used and results in a 30 K bandgap energy ($E_p = 327.2$ meV) specified by the peak position (328.5 meV) less $kT/2$ (1.3 meV). On the other hand, using the first derivative maximum, a 30 K bandgap energy ($E_g = 324.5$ meV) is identified that is 2.7 meV smaller. The significance of the first derivative maximum method is that it indicates the energy at which the product of the optical joint density of states and photon occupation number increases at the greatest rate. Since the optical joint density of states rapidly increases at the onset of optical transitions involving the electron and hole continuum band edges (i.e., at the bandgap) and the occupation number decreases at a slower rate, the analysis has good sensitivity to the bandgap position and is less sensitive to injection level. As can be seen in the inset of Fig. 2, the first derivative peak position is insensitive to the carrier excitation rate and hence the carrier occupation.

The $InAs_{0.911}Sb_{0.089}$ bandgap energies as a function of temperature are shown in Fig. 3 where the values given by the photoluminescence peak position minus $kT/2$ (E_p) are specified by the solid and open circles and those given by the first derivative maximum (E_g) are specified by the solid and open squares. Room temperature photoluminescence is observed, however the bandgap energy cannot be accurately identified as the photoluminescence peak occurs near 290 meV where there is a strong CO_2 absorption feature in the spectra. In its place, the room temperature bandgap energy determined by spectroscopic ellipsometry is shown with a solid diamond at 295 K. The solid curves in Fig. 3 are fits of the Einstein single oscillator model[15,16] (Equation (1)) to the temperature dependent data: T is the absolute temperature, k is the Boltzmann constant (0.0862 meV/K), and the fitting parameters are E_0 the 0 K bandgap energy, T_E the Einstein temperature, and S_0 the dimensionless coupling parameter, where S_0k is the slope of the high temperature linear asymptote

$$E(T) = E_0 - \frac{S_0 k T_E}{\exp(T_E/T) - 1}. \quad (1)$$

The best fit parameters for the bandgaps specified by each method (E_p and E_g) are, respectively, 327.4 and 324.6 meV for E_0, 298.5 and 240.3 K for T_E, and 3.10 and 2.96 for S_0. For both methods, the open circle and square at 15 K are omitted from the fit as the decrease in bandgap energy with decreasing temperature is likely a result of a small degree of compositional inhomogeneity in the alloy. The Einstein single oscillator best fit parameters are summarized in Table I; in addition to those mentioned above, the parameters with the room

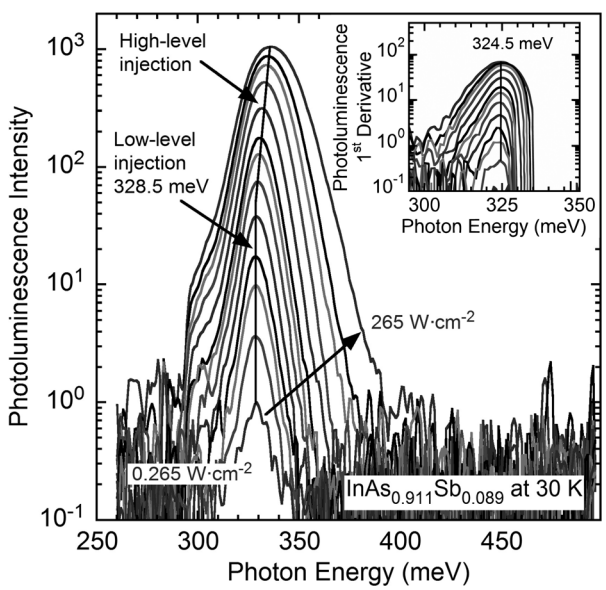

FIG. 2. Photoluminescence spectra from lattice-matched $InAs_{0.911}Sb_{0.089}$ on GaSb at 30 K, measured using pump power densities ranging from 0.265 to 265 W cm^{-2}. The photoluminescence peak position is independent of pump power under low injection (0.265–2.65 W cm^{-2}) and blue shifts under high injection (2.65–265 W cm^{-2}). The inset shows the first derivative of the spectra and the position of their maxima (vertical line).

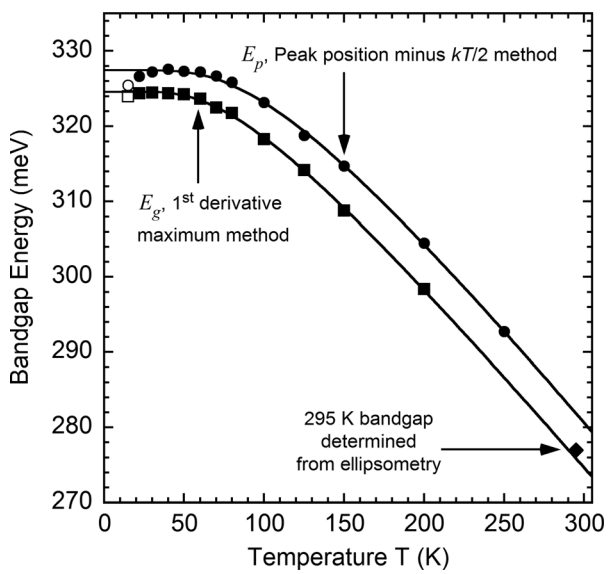

FIG. 3. Bandgap energy as a function of temperature for lattice-matched $InAs_{0.911}Sb_{0.089}$ on GaSb determined from the photoluminescence peak energy minus $kT/2$ (E_p, circles) and the first derivative maximum of the photoluminescence spectra (E_g, squares). The Einstein single oscillator model (solid curves) is fit to the bandgap data. The room temperature bandgap energy (diamond) determined from the absorption cutoff measured by spectroscopic ellipsometry is shown for comparison.

temperature value included are shown in the last row of the table. It is worth noting that the 327.4 meV value for E_0 is determined using the photoluminescence peak position minus $kT/2$ is consistent with the bandgap value of 327 meV for $InAs_{0.9}Sb_{0.1}$ determined using the same method in Ref. 8. The advantage of the first derivative method is that it systematically identifies the bandgap energy for both emission and absorption measurements as it is sensitive to the underlying material band structure; note the agreement of photoluminescence and ellipsometry experiments shown in Fig. 3.

Since the Varshni equation[17] (Equation (2)) is commonly used to describe the temperature dependence of the bandgap energy in these materials,[4] the Einstein single oscillator model (solid curve) and the Varshni equation (dotted and dashed curves) are compared in Fig. 4 by way of best fits to the bandgap measurements, E_g, determined using the first derivative method (solid squares). This is same data shown in Fig. 3 with the inclusion of the room temperature value determined by spectroscopic ellipsometry. The fit parameters are compared in Table II, where the zero temperature bandgap is E_0 for both models, the high temperature linear slope is α for the Varshni equation and S_0k for the single oscillator model, the position of the knee (intersection of the zero temperature bandgap energy and the high temperature linear asymptote) is β for the Varshni equation and $\frac{1}{2}T_E$ for the single oscillator model, and the bandgap reduction due to the zero-point motion of the lattice is $\alpha\beta$ for the Varshni equation and $\frac{1}{2}S_0kT_E$ for the single oscillator model

$$E(T) = E_0 - \frac{\alpha T^2}{T+\beta}. \tag{2}$$

The functional form of the empirical Varshni equation (dotted curve) does not describe the bandgap data in Fig. 4 nearly as well as the physical Einstein single oscillator model (solid curve), particularly for the low temperature data where the Varshni equation is quadratic. This quadratic behavior overestimates the value of the low temperature bandgap and underestimates the curvature of the knee region where the thermal phonon occupation first starts to significantly shift the bandgap with temperature. Furthermore, the Varshni equation does not capture the linear dependence of bandgap at room temperature and beyond. When the low temperature data are excluded the Varshni equation more accurately identifies the linear dependence of bandgap at room temperature, as illustrated by the dashed curve in Fig. 4 fit to the data for temperatures above 80 K. The limitations of the Varshni equation have been previously noted by several authors.[18–20] The issue confronting empirical models is that it essentially takes four parameters to describe the temperature dependence of the bandgap energy: (i) the low temperature bandgap, (ii) the position of knee, (iii) the curvature of the knee, and (iv) the high temperature slope. Fitting a 4-parameter empirical model is shown to work well for many III-V materials.[18] However, since the Einstein single oscillator is a physical model, it precisely describes the temperature dependence of the bandgap using three fitting parameters, as the shape of the knee is effectively described by the functional form of the physical model.

In order to determine the bandgap of $InAs_{1-x}Sb_x$ as a function of temperature and Sb mole fraction x, the bandgap bowing parameter $b_g(T)$ in Equation (3) is fit as a function of temperature to the bandgaps of $InAs_{0.911}Sb_{0.089}$, InAs, and InSb. The resulting low and room temperature bandgap bowing parameters of 938 meV at 0 K and 750 meV at 295 K are obtained using the low and room temperature bandgaps of $InAs_{0.911}Sb_{0.089}$, InAs, and InSb; $E_{g\,InAsSb}(0.0891,T)$ is

TABLE I. Bandgap temperature dependence parameters (E_0, S_0, and T_E) for $InAs_{0.911}Sb_{0.089}$ as determined from the peak position minus $kT/2$ method (E_p) and the first derivative maximum method (E_g). For the first derivative maximum method, the fit is performed with and without the room temperature bandgap determined from spectroscopic ellipsometry.

Method	E_0 (meV)	S_0	T_E (K)
Peak minus $kT/2$, E_p	327.4	3.10	298.5
First derivative maximum, E_g (without room temperature data)	324.6	2.96	240.3
First derivative maximum, E_g (with room temperature data)	324.7	2.85	230.7

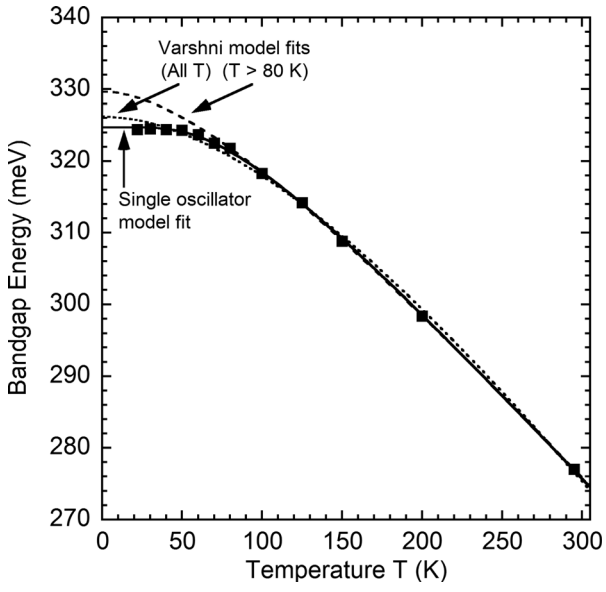

FIG. 4. Bandgap energy as a function of temperature for lattice-matched $InAs_{0.911}Sb_{0.089}$ on GaSb determined using the first derivative maximum method. The Einstein single oscillator model is shown as the solid curve and the Varshni equation as the dotted curve (all temperatures) and dashed curve (temperatures greater than 80 K).

TABLE II. Comparison of the Einstein single oscillator model and Varshni equation fits to the temperature dependence of the $InAs_{0.911}Sb_{0.089}$ bandgap energy. The low temperature bandgap energy is E_0 for both models, the linear bandgap reduction rate in the high temperature region is α for the Varshni equation and S_0k for the single oscillator model, the intersection of the zero temperature bandgap energy and high temperature asymptote is β for the Varshni equation and $\frac{1}{2}T_E$ for the single oscillator model, and the bandgap reduction due to the zero-point motion of the lattice is $\alpha\beta$ for the Varshni equation and $\frac{1}{2}S_0kT_E$ for the single oscillator model.

Model	E_0 (meV)	S_0k; α (meV/K)	$\frac{1}{2}T_E$; β (K)	$\frac{1}{2}S_0kT_E$; $\alpha\beta$ (meV)
Einstein single oscillator	324.7	0.246	115.4	28.3
Varshni equation (All T)	326.2	0.359	335.0	120.3
Varshni equation (T > 80 K)	329.7	0.256	128.1	32.8

TABLE III. Bandgap temperature dependent parameters (E_0, S_0, and T_E) for bulk InAs and InSb.

Material	E_0 (meV)	S_0	T_E (K)
InAs	417	3.20	145.0
InSb	235	3.13	133.0

324.7 meV at 0 K and 277.0 meV at 295 K (this work), $E_{g\,InAs}(T)$ is 417.0 meV[4] at 0 K and 354.0 meV (this work) at 295 K, and $E_{g\,InSb}(T)$ is 235.0 meV[4] at 0 K and 172.0 meV (this work) at 295 K. The room temperature bandgap energies of InAs and InSb are determined from spectroscopic ellipsometry measurements of InAs and InSb substrates analyzed in a similar manner to that for $InAs_{0.911}Sb_{0.089}$ shown in Fig. 1, and are consistent with those values reported in Refs. 4 and 21 of 355 and 352 meV for InAs and 175 and 176 meV for InSb. The temperature dependence of the bandgaps $E_{g\,InSb}(T)$ and $E_{g\,InAs}(T)$ in Equation (3) is described by the single oscillator model given in Equation (1). The resulting oscillator model parameters are listed in Table III where E_0 is the low temperature bandgap most commonly reported in Ref. 4, S_0 is the coupling parameter obtained from the high temperature linear asymptotes in Ref. 21, and T_E is fit to obtain the bandgap energies measured by spectroscopic ellipsometry at room temperature. The temperature dependence of the bowing parameter $b_g(T)$ is accurately described using the double oscillator model in Equation (4), with the resulting parameters shown in Table IV

$$E_{g\,InAsSb}(x,T) = x \cdot E_{g\,InSb}(T) + (1-x) \cdot E_{g\,InAs}(T) - x(1-x)b_g(T), \quad (3)$$

$$b_g(T) = b_0 - \frac{S_1 k T_1}{\exp(T_1/T) - 1} + \frac{S_2 k T_2}{\exp(T_2/T) - 1}. \quad (4)$$

In Section III, the InAs/InAsSb superlattice low and room temperature ground state transition energies (effective bandgaps) are determined from low temperature photoluminescence and room temperature spectroscopic ellipsometry measurements. Further analysis using these and the InAsSb bandgap measurements above provides the low and room temperature band offsets for the InAs/InAsSb superlattice system.

III. ELLIPSOMETRY AND PHOTOLUMINESCENCE OF InAs/InAsSb SUPERLATTICES

The strain-balanced InAs/InAsSb superlattice samples studied are grown by molecular beam epitaxy on (100)-oriented $\frac{1}{4}$ and full 50 mm GaSb substrates and are evaluated using X-ray diffraction, photoluminescence spectroscopy, and spectroscopic ellipsometry. The superlattice structures are composed of alternating thin layers of InAs and InAsSb with a total thickness of 0.5 to 11 μm sandwiched between 10 nm thick AlSb confinement layers with a 10 nm thick GaSb or InAs cap. The growth is performed using constant In and As fluxes with the superlattice defined by modulating the Sb flux with the Sb shutter that is closed during the InAs layer and open during the InAsSb layer. For all samples, the In flux is held constant throughout the structure at around 0.5 monolayers per second with a constant As/In flux ratio of 1.20, whereas the Sb/In flux ratio ranges from 0.25 to 2.00 for the various samples and is the determining factor for the Sb mole fraction. For an As/In flux ratio of 1.20, the sticking coefficient of Sb is about 40% for a growth temperature of 430 °C;[22] the sticking coefficient is temperature dependent and, in particular, significantly decreases for higher temperature growths.

TABLE IV. Bandgap bowing parameter temperature dependent parameters (b_0, S_1, T_1, S_2, and T_2) for bulk InAsSb.

Material	b_0 (meV)	S_1	T_1 (K)	S_2	T_2 (K)
InAsSb	938	22.98	115.8	18.80	275.6

The structural properties of the superlattices are determined using commercial dynamical X-ray diffraction software[10] and a self-consistent analysis of coupled ω-2θ X-ray diffraction scans from the (004)-planes of each sample. In this analysis, the satellite peak spacing determines the superlattice period thickness while the 0th order satellite peak position, the Sb shutter times, and the InAs and InAsSb growth rates determine the Sb mole fraction and constituent layer thicknesses. This conventional approach to modeling the X-ray data results in the first set of structural parameters shown in part 3 of Table V.

Moreover, it is observed that the InAs/InAsSb interfaces are not perfectly abrupt due to the surface segregation of Sb that is subsequently incorporated into the InAs layer after the Sb shutter is closed.[23–26] Therefore, to evaluate the impact of unintentional Sb in the InAs layer, the X-ray diffraction data are further analyzed using a model with a small amount of Sb in the InAs layer. Under the strain-balanced condition, this results in a reduced level of tensile strain in the InAs layer and corresponding larger reduction in the compressive strain of the InAsSb layer that is typically not as thick as the InAs layer. During this analysis, it is observed that the relative intensities of the satellite peaks are sensitive to changes in the strain and the thicknesses of the constituent layers, as this influences the structure factor for the diffraction condition of the satellite peaks.[27] Therefore, in addition to those parameters fit above, the average unintentional Sb mole fraction of the InAs layer is fit to the intensity profile of the satellite peaks.

In particular, a great deal of sensitivity is obtained when one or more satellite peaks are very weak as a result of strong destructive interference for the specific structure. This is shown in Fig. 5, which compares the X-ray diffraction pattern of sample E (grey curves) to the diffraction patterns simulated using average unintentional Sb mole fractions of 0.004, 0.006, and 0.008 in the InAs layers (black curves). Of particular interest are the 0th order satellite peaks SL_0 and the 4th order satellite peaks SL_4 that exhibit a much lower intensity than the other satellite peaks. The simulated intensity of these peaks is very sensitive to small changes of the Sb mole fraction in the InAs layer. The model simulation with an average unintentional Sb mole fraction of 0.006 provides the best fit to the overall intensity profile of sample E with an InAsSb layer mole fraction of 0.322, an InAsSb layer

TABLE V. Growth temperature (1), optical properties (2), and structural properties (3 and 4) of the InAs/InAsSb superlattices investigated. The bandgap energies are measured by spectroscopic ellipsometry at room temperature and photoluminescence spectroscopy at low temperature. The structural parameters are determined by room temperature X–ray diffraction measurements, where the analysis utilizes a model without (3) and with (4) the incorporation of unintentional Sb in the InAs layer.

	(1)	(2) First derivative maximum method		(3) Structural parameters: Assuming no unintentional Sb in InAs			(4) Structural parameters: Including unintentional Sb in InAs			
Sample	Growth temp. (°C)	295 K transition energy (meV)	12 K transition energy (meV)	Sb mole fraction x	InAs layer thickness (nm)	$InAs_{1-x}Sb_x$ layer thickness (nm)	Average unintentional Sb mole fraction in InAs	Sb mole fraction x	InAs layer thickness (nm)	$InAs_{1-x}Sb_x$ layer thickness (nm)
A	400	260	311	0.130	5.13	4.61	0.012	0.117	5.14	4.60
B	405	103	156	0.284	17.18	7.32	0.008	0.263	17.16	7.34
C	410	76	128	0.312	18.64	5.70	0.006	0.291	18.66	5.68
D	450	136	…	0.328	8.19	2.52	0.014	0.279	8.21	2.50
E	410	74	122	0.343	15.21	4.67	0.006	0.322	15.23	4.65
F	410	56	98	0.360	18.59	5.72	0.006	0.338	18.60	5.70
G	410	51	102	0.367	15.29	4.71	0.006	0.345	15.31	4.69
H	410	64	106	0.370	14.83	4.56	0.006	0.348	14.84	4.56
I	410	107	162	0.392	7.93	2.46	0.012	0.351	7.94	2.45
J	400	68	134	0.400	8.31	2.58	0.010	0.367	8.31	2.57

thickness of 4.65 nm, and an InAs layer thickness of 15.23 nm.

The best fit structural parameters and average unintentional Sb mole fractions of samples A-J are summarized in part 4 of Table V. The average unintentional Sb mole fractions are about 0.006 for 15 and 18 nm thick InAs layers and are approximately double for the 5 to 8 nm thick InAs layers. The unintentional Sb is mainly incorporated near to the InAs-on-InAsSb interface[24,25] and hence decreases as the layer grows. In the assessment of the superlattice band offsets in Section IV, the structural parameters that account for unintentional Sb incorporation into InAs (part 4 of Table V) are utilized.

Photoluminescence from the InAs/InAsSb superlattice sample set is measured at 12 K using 68 mW of pump power from an 808 nm laser; this results in 90 W cm^{-2} of pump power arriving at the upper superlattice interface and a carrier excitation density of 7.1×10^{24} cm^{-3} s^{-1}. The maxima of the first derivative of the photoluminescence spectra are computed to determine the 12 K ground state transition energy (effective bandgap) for each sample. The normalized photoluminescence spectra of samples A, B, E, and F are plotted in Fig. 6 as a function of photon energy (lower horizontal axis) and photon wavelength (upper horizontal axis). The vertical dotted lines show the ground state energy for

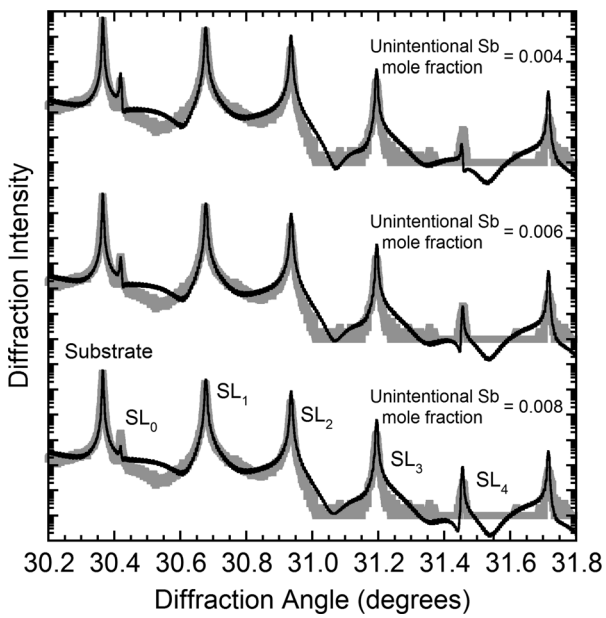

FIG. 5. Measured X-ray diffraction pattern of InAs/InAsSb superlattice sample E (grey curves) alongside diffraction patterns simulated using a structure model with average unintentional Sb mole fractions of 0.004, 0.006, and 0.008 in the InAs layers of the superlattice (black curves).

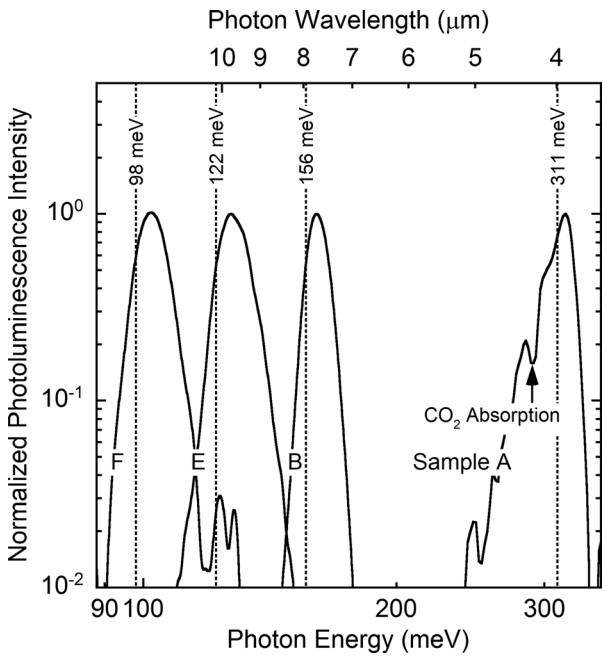

FIG. 6. Normalized 12 K photoluminescence spectra from InAs/InAsSb superlattice samples A, B, E, and F. The superlattice ground state transition energies identified from the maximum of the first derivative of the photoluminescence spectra are indicated by vertical dotted lines.

each sample. The ground state transition energies are listed in part 2 of Table V for the entire sample set expect for sample D where the photoluminescence signal is too noisy to accurately distinguish the first derivative maximum.

The room temperature ground state transition energies of the superlattice samples are identified from the absorption coefficient spectra using the first derivative maximum method that identifies the rapid increase in the optical joint density of states at the ground state transition of the superlattice. The room temperature bandgap energies determined using spectroscopic ellipsometry are summarized in part 2 of Table V; additional details and conclusions from the spectroscopic ellipsometry measurements of the InAs/InAsSb superlattice sample set can be found in Ref. 2.

IV. BAND OFFSET RESULTS AND DISCUSSION

A Kronig-Penney model of the superlattice miniband structure[28,29] is used to determine the ground state transition energies of each sample listed in Table V using the bulk InAs and InAsSb parameters provided in Table VI. These transition energies are established between the ground state electron and heavy hole minibands that form in the repeating potential of the strained band alignment of the InAs/InAsSb superlattice layers. Within the model, the strained valence band offset, $\Delta E_v(x)$, between the $InAs_{1-x}Sb_x$ heavy hole valence band edge, $E_v(x)$, and the InAs heavy hole band edge, $E_v(0)$ (see the inset of Fig. 7), is a fitting parameter employed to align the calculated transition energies to those experimentally measured for each sample. The strained valence band offsets, $\Delta E_v(x) = E_v(x) - E_v(0)$, determined at low temperature (black squares) and room temperature (black circles) are plotted as a function of Sb mole fraction in Fig. 7.

The valence band offset bowing model shown in Equation (5) is fit to the strained data in Fig. 7; the best fits are shown as the dotted black curve for the low temperature result and the solid black curve for the room temperature result. Since the valence band edges of InAs and InSb, $E_v(0)$ and $E_v(1)$, are known,[4,30,31] the valence band bowing parameter, b_v, is a fitting parameter whose best fit values are given in Table VII. The unstrained curves (solid and dotted grey curves) are determined by backing out the effects of the InAs tensile strain and the InAsSb compressive strain on the valence band offsets using the Pikus-Bir Hamiltonian.[30,31] The resulting low and room temperature unstrained band alignment is shown in Fig. 8

$$\Delta E_v(x) = x\Delta E_v(1) - x(1-x)b_v. \tag{5}$$

The valence band bowing parameters (b_v) determined in Fig. 7, the bandgap bowing parameters (b_g) determined in Section II, and the resulting conduction band bowing parameters given by $b_c = b_v + b_g$, are summarized in Table VII. The band bowing is upward (negative) for the valence band and downward (positive) for the conduction band, with a resultant downward (positive) bowing for the bandgap. Fig. 8 shows the unstrained band edge positions of InAsSb as a function of mole fraction; in the absence of strain, InAsSb

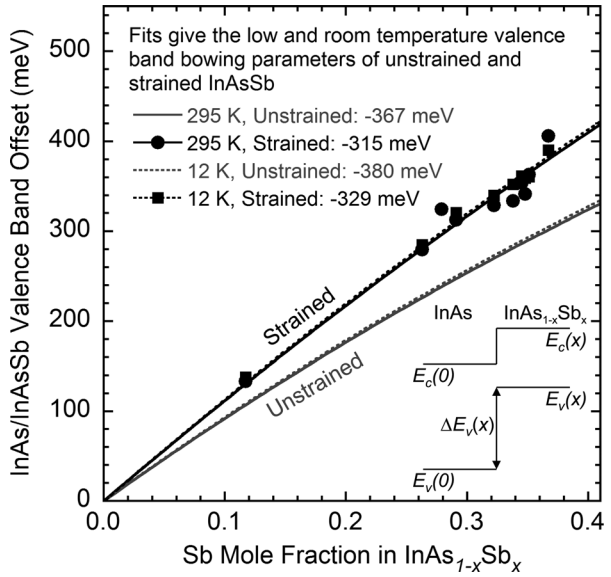

FIG. 7. Heavy hole valence band offset of $InAs_{1-x}Sb_x$ relative to InAs, $\Delta E_v(x)$, plotted as a function of Sb mole fraction at 295 K (circles) and 12 K (squares). The solid (room temperature) and dotted (low temperature) black curves represent bowing model fits to the strained band offset data. The analysis for unstrained bulk material is shown as solid (room temperature) and dotted (low temperature) grey curves obtained by backing out the effect of strain.

TABLE VI. Material parameters of InAs and InSb used in the Kronig-Penney model of the InAs/InAsSb superlattice miniband structure. The bandgaps and valence band offsets of InAsSb are calculated using the bowing parameters provided in Table VII and the electron effective mass is calculated using a bowing parameter of 0.035;[4] all other parameters are assumed to vary linearly with mole fraction between the respective values of InAs and InSb. The room temperature bandgap values are from this work and all other parameter values are taken from Ref. 4.

Material parameter	InAs	InSb
Low temperature bandgap (meV)	417	235
Room temperature bandgap (meV)	354	172
Low and room temperature valence band offset (meV)	−590	0
Poisson's ratio	0.3521	0.3530
Conduction band deformation potential (eV)	−5.08	−6.94
Valence band deformation potential (eV)	−1.00	−0.36
Shear deformation potential (eV)	−1.80	−2.00
Electron effective mass	0.0260	0.0135
Heavy hole effective mass	0.3333	0.2632
Lattice constant (nm)	0.60582	0.64792

TABLE VII. Bowing parameters for the bandgap (b_g), valence band (b_v), and conduction band (b_c) of unstrained bulk InAsSb and coherently strained InAsSb on GaSb.

		First derivative maximum method	
		at 295 K (meV)	at 12 K (meV)
Unstrained	b_g	750	938
	b_v	−367	−380
	b_c	383	558
Strained	b_g	783	971
	b_v	−315	−329
	b_c	468	642

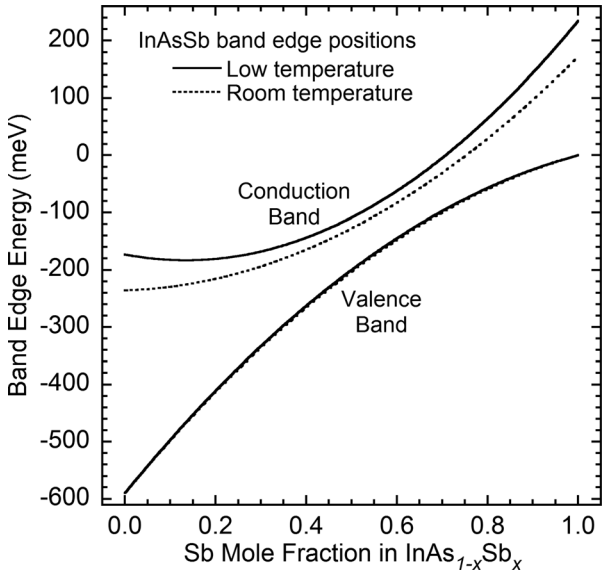

FIG. 8. Conduction and valence band edge positions relative to the InSb valence band for unstrained bulk InAsSb at low (solid curve) and room (dotted curve) temperature.

forms a weak type-I band alignment with InAs for low Sb mole fractions and a type-II band alignment at higher mole fractions. The percentage of the total bandgap bowing attributed to the valence band at low temperature is 41%, which is consistent with what has been reported by other authors.[32,33]

When the material is coherently strained the band bowing decreases in the valence band and increases in the conduction band and bandgap. In general, for ternary materials, the shift in the band edges with biaxial strain is not linear as the strain, the deformation potentials, and Poisson's ratio all are typically functions of mole fraction. In coherently strained InAsSb on GaSb, the variation in the deformation potentials with mole fraction is the dominant factor that modifies the strained bowing parameters. In the conduction band, for example, the conduction band deformation potential changes from −5.08 eV for InAs to −6.94 eV for InSb. As a result, the strained conduction band edge moves to higher energies with increasing Sb mole fraction at a greater rate than it would if the deformation potential were constant. The same is true in the valence band which is modified by a combination of the valence band and shear deformation potentials. This results in a larger strained band offset bowing parameter and a stronger type-II band alignment in strain-balanced InAs/InAsSb.

Had the structural parameters that assume no unintentional Sb incorporation (part 3 of Table V) been used for this analysis, the measured band offsets would remain virtually unchanged; however, the Sb mole fractions of the InAsSb layers would all increase by 0.01 to 0.05. This would induce a horizontal right shift in the data in Fig. 7 that would result in a significant change in the distribution of the band offset bowing; in particular, 12% of the bandgap bowing would transfer from the valence band to the conduction band at low temperature and 18% at room temperature. These results indicate that the unintentional incorporation of Sb into the InAs layers should not be ignored in this analysis.

TABLE VIII. Low and room temperature ground state transition energies of InAs/InAsSb type-II superlattices. The experimental values are determined using photoluminescence spectroscopy at low temperature and spectroscopic ellipsometry at room temperature (see Table V), and the calculated values are determined using a Kronig-Penney model and the material parameters detailed in Tables VI and VII.

	Low temperature transition energies (meV)		Room temperature transition energies (meV)	
Sample	Experimental	Calculated	Experimental	Calculated
A	311	314.0	260	261.5
B	156	157.5	103	102.2
C	128	136.5	76	80.3
D	…	207.9	136	156.0
E	122	121.0	74	65.9
F	98	94.8	56	38.4
G	102	101.0	51	45.8
H	106	100.5	64	45.5
I	162	156.6	107	105.5
J	134	139.4	68	87.9

The InAsSb bandgap and band edge bowing parameters in Table VII are programmed into the Kronig-Penney software model, allowing more accurate miniband structure calculations to be performed. Table VIII compares the superlattice ground state transition energies detailed in Table V alongside the transition energies calculated in the updated Kronig-Penney model. Close agreement is obtained between theory and experiment, ultimately indicating that this software tool is capable of making accurate band structure predictions, which could be used to identify optimized superlattice designs.

V. CONCLUSIONS

Several InAs/InAsSb superlattices are examined that have period thicknesses ranging from 10 to 25 nm, Sb mole fractions ranging from 12% to 37%, and bandgap energies that range from 98 to 311 meV (12.7–4.0 μm) at low temperature and 51 to 260 meV (24.3–4.8 μm) at room temperature. An average unintentional incorporation of ∼1% Sb in the InAs layer is taken into consideration in the analysis. The InAs/InAsSb band offset for each sample composition is obtained from analysis of the superlattice ground state energy and miniband structure and measurements of the bandgap energy of bulk $InAs_{0.911}Sb_{0.089}$. The composition dependent InAsSb bandgap and InAs/InAsSb band edge positions are parameterized using bowing models, where the low and room temperature bowing parameters are, respectively, 558 and 383 meV for the conduction band edge, −380 and −367 meV for the valence band edge, and 938 and 750 meV for the InAsSb bandgap. Ignoring the small amount of unintentional Sb in the InAs layer results in a significant change in the observed band offset bowing; in which case, the fraction of bandgap bowing displaced from the valence to the conduction band would be 12% at low temperature and 18% at room temperature.

ACKNOWLEDGMENTS

The authors acknowledge the financial support of the U.S. Army Research Office MURI program, Grant No.

W911NF-10-1-0524. The authors also acknowledge the use of facilities in the LeRoy Eyring Center for Solid State Science at Arizona State University.

[1]Y.-H. Zhang, Appl. Phys. Lett. **66**, 118 (1995).
[2]P. T. Webster, N. A. Riordan, S. Liu, E. H. Steenbergen, R. A. Synowicki, Y.-H. Zhang, and S. R. Johnson, Appl. Phys. Lett. **106**, 061907 (2015).
[3]A. G. Thompson and J. C. Woolley, Can. J. Phys. **45**, 255 (1967).
[4]I. Vurgaftman, J. R. Meyer, and L. Ram-Mohan, J. Appl. Phys. **89**, 5815 (2001).
[5]M. Y. Yen, R. People, and K. W. Wecht, J. Appl. Phys. **64**, 952 (1988).
[6]C. G. Bethea, B. F. Levine, M. Y. Yen, and A. Y. Cho, Appl. Phys. Lett. **53**, 291 (1988).
[7]D. Wang, Y. Lin, D. Donetsky, L. Shterengas, G. Kipshidze, G. Belenky, W. L. Sarney, H. Hier, and S. P. Svensson, Proc. SPIE **8353**, 835312-1 (2012).
[8]S. P. Svensson, W. L. Sarney, H. Hier, Y. Lin, D. Wang, D. Donetsky, L. Shterengas, G. Kipshidze, and G. Belenky, Phys. Rev. B **86**, 245205 (2012).
[9]E. H. Steenbergen, O. O. Cellek, D. Lubyshev, Y. Qiu, J. M. Fastenau, A. W. K. Liu, and Y.-H. Zhang, Proc. SPIE **8268**, 82680K (2012).
[10]X'pert Epitaxy software, PANalytical B. V., Almelo, The Netherlands.
[11]IR-VASE system, J. A. Woollam Co. Inc., Lincoln, NE, USA.
[12]M. Schubert, *Infrared Ellipsometry on Semiconductor Layer Structures: Phonons, Plasmons, and Polaritons* (Springer, Heidelberg, 2004), p. 21.
[13]E. F. Schubert, *Light-Emitting Diodes* (Cambridge University Press, New York, 2007), pp. 87–90.
[14]F. Urbach, Phys. Rev. **92**, 1324 (1953).
[15]S. R. Johnson and T. Tiedje, J. Appl. Phys. **78**, 5609 (1995).
[16]L. Viña, S. Logothetidis, and M. Cardona, Phys. Rev. B **30**, 1979 (1984).
[17]Y. P. Varshni, Physica (Utrecht) **34**, 149 (1967).
[18]R. Pässler and G. Oelgart, J. Appl. Phys. **82**, 2611 (1997).
[19]S. A. Lourenço, I. F. L. Dias, J. L. Duarte, E. Laureto, E. A. Meneses, J. R. Leite, and I. Mazzaro, J. Appl. Phys. **89**, 6159 (2001).
[20]R. Pässler, J. Appl. Phys. **89**, 6235 (2001).
[21]Z. M. Fang, K. Y. Ma, D. H. Jaw, R. M. Cohen, and G. B. Stringfellow, J. Appl. Phys. **67**, 7034 (1990).
[22]P. T. Webster, N. A. Riordan, C. Gogineni, S. Liu, J. Lu, X.-H. Zhao, D. J. Smith, Y.-H. Zhang, and S. R. Johnson, J. Vac. Sci. Technol. B **32**, 02C120 (2014).
[23]B. R. Bennett, B. V. Shanabrook, R. J. Wagner, J. L. Davis, and J. R. Waterman, Appl. Phys. Lett. **63**, 949 (1993).
[24]A. Y. Lew, E. T. Yu, and Y.-H. Zhang, J. Vac. Sci. Technol. B **14**, 2940 (1996).
[25]L. Ouyang, E. H. Steenbergen, Y.-H. Zhang, K. Nunna, D. L. Huffaker, and D. J. Smith, J. Vac. Sci. Technol. B **30**, 02B106 (2012).
[26]M. R. Wood, K. Kanedy, F. Lopez, M. Weimer, J. F. Klem, S. D. Hawkins, E. A. Shaner, and J. K. Kim, J. Cryst. Growth **425**, 110 (2015).
[27]V. S. Speriosu and T. Vreeland, Jr., J. Appl. Phys. **56**, 1591 (1984).
[28]H.-S. Cho and P. R. Prucnal, Phys Rev. B **36**, 3237 (1987).
[29]S.-H. Pan and S.-M. Feng, Phys. Rev. B **44**, 5668 (1991).
[30]G. L. Bir and G. E. Pikus, *Symmetry and Strain-Induced Effects in Semiconductors* (Wiley, New York, 1974).
[31]S. L. Chuang, *Physics of Optoelectronic Devices* (Wiley, New York, 1995), pp. 655–661.
[32]D. Lackner, O. J. Pitts, M. Steger, A. Yang, M. L. W. Thewalt, and S. P. Watkins, Appl. Phys. Lett. **95**, 081906 (2009).
[33]Y. Lin, D. Wang, D. Donetsky, L. Shterengas, G. Kipshidze, G. Belenky, S. P. Svensson, W. L. Sarney, and H. Hier, J. Electron. Mater. **42**, 918 (2013).